Chinese Chemical Letters 35 (2024) 109255

Contents lists available at ScienceDirect

Chinese Chemical Letters

journal homepage: www.elsevier.com/locate/cclet

Cubic S/N co-doped TiO_2 with rich oxygen vacancies from Ti-MOFs for efficient elimination of formaldehyde

Qing Gao[a,1], Lei Sun[a,1], Zhihua Wang[a,*], Jiguang Deng[b,*]

[a] State Key Laboratory of Chemical Resource Engineering, Beijing University of Chemical Technology, Beijing 100029, China
[b] Beijing Key Laboratory for Green Catalysis and Separation, Key Laboratory of Beijing on Regional Air Pollution Control, Key Laboratory of Advanced Functional Materials, Education Ministry of China, Department of Chemical Engineering, Beijing University of Technology, Beijing 100124, China

ARTICLE INFO

Article history:
Received 3 February 2023
Revised 26 October 2023
Accepted 26 October 2023
Available online 28 October 2023

Keywords:
Metal-organic frameworks
Photocatalysis
Formaldehyde removal
S/N co-doped TiO_2
Oxygen vacancies

ABSTRACT

The cubic S/N co-doped TiO_2 (TNS*x*, *x* is the calcination temperature) photocatalysts with rich oxygen vacancies were obtained by high temperature calcination of sulfur powder and titanium-based MOFs NH_2-MIL-125 for the photocatalytic removal of gaseous formaldehyde (a volatile organic compound). Among the obtained catalysts, the presence of oxygen vacancies restricted photogenerated electron and holes recombination. 98.00% removal of gaseous formaldehyde in 150 min could be achieved over TNS600 by xenon lamp. The removal efficiency for formaldehyde was well retained for five cycle experiment. The results from PL, TRPL and EIS revealed that TNS600 had the best separation efficiency of photogenerated electrons and holes, and the enhanced charge separation led to a significant increase in photocatalytic activity. The photocatalytic oxidation mechanism indicated that the $^{\bullet}OH$ and $^{\bullet}O_2^-$ radicals were mainly involved in the efficient elimination of gaseous formaldehyde and were able to mineralize formaldehyde to H_2O and CO_2.

In recent years, the natural environment, including the atmospheric quality has been incessantly destroyed due to the human production activities [1]. Volatile organic compounds (VOCs), with high-risk biological toxicity, not only seriously threaten human health, but also play a key role in atmospheric chemistry, giving the formation of ozone, secondary organic aerosols, and the greenhouse effect [2]. Therefore, the removal of VOCs has become one of the hot spots in recent years. Among the various VOCs, formaldehyde (HCHO) from building materials, fabrics, adhesives, paints and coatings is one of the most toxic gases that humans are easily exposed [3]. Trace amount of HCHO might cause respiratory and eye symptoms, and high concentrations or prolonged exposure even trigger for some cancers [4].

Compared with traditional treatment methods, photocatalytic oxidation possesses the advantage such as mild reaction condition and low energy cost [5]. However, this method also suffers from the low efficiency of photogenerated electron-hole separation. The introduction of oxygen vacancies into the metal oxide photocatalyst improves photogenerated charge migration and photogenerated carrier separation, and then enhances photocatalytic efficiency [6]. TiO_2 is one of the most popular photocatalysts, while the rapid recombination of photogenerated carriers and the loss of active sites caused by agglomeration of spherical particles, limit its application prospects [7]. Previous studies indicate that the element doping strategy could endow TiO_2 with high carrier separation efficiency and narrow band gap, and the elements that could be chosen for doping include metal and nonmetal elements [8]. Nonmetal element (*e.g.*, C, N, S, and/or P) doping has been widely studied due to its easy availability and the more facile doping conditions. Various doping materials based on TiO_2 have been reported, such as S-TiO_2, N-TiO_2, P-TiO_2, F-TiO_2, C-TiO_2, and N/S-TiO_2 [8,9].

Metal-organic frameworks (MOFs) show wide applications in the field of photocatalysis, due to their controllable morphology and abundant active sites [10]. NH_2-MIL-125, as a representative of Ti-based MOFs, has excellent visible light utilization ability because of the introduction of amino [11,12]. More interestingly, the preparation of derivation using MOFs as precursors *via* the calcination process is a promising direction. The derivations might keep the morphology and high specific surface area of the MOFs precursors [13]. TiO_2-based materials derived from NH_2-MIL-125 have shown great potential in the field of photocatalytic oxidation [14]. In the present study, the S/N co-doped TiO_2 (TNS*x*, *x* is the calcination temperature, and T600 was synthesized *via* the calcination

* Corresponding authors.
E-mail addresses: zhwang@mail.buct.edu.cn (Z. Wang), jgdeng@bjut.edu.cn (J. Deng).
[1] These authors contributed equally to this work.

https://doi.org/10.1016/j.cclet.2023.109255
1001-8417/

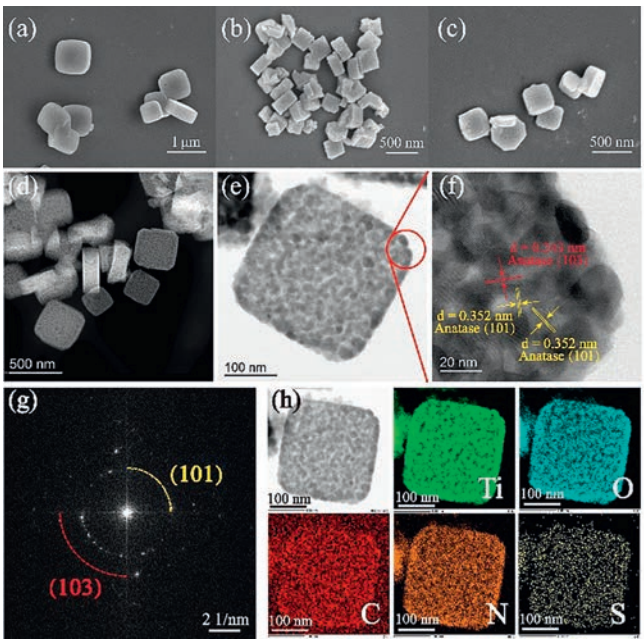

Fig. 1. SEM of (a) NH_2-MIL-125, (b) T600, (c) TNS600. (d-f) HRTEM and (g) SAED of TNS600. (h) Elemental mappings of the TNS600.

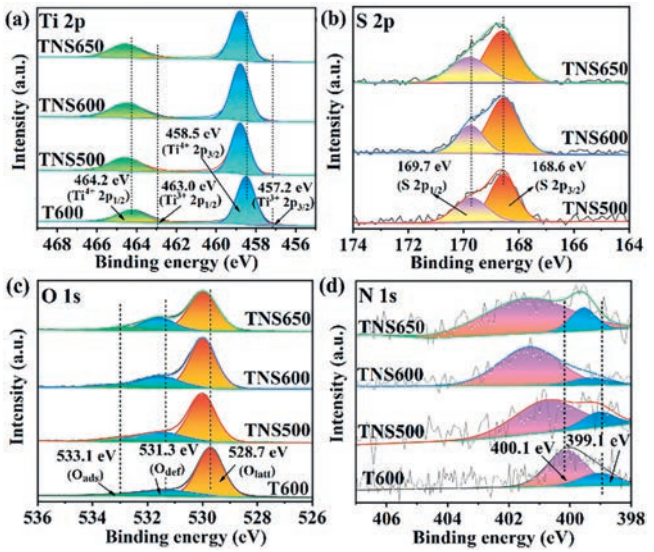

Fig. 2. (a) Ti 2p, (b) S 2p, (c) O 1s, and (d) N 1s XPS spectra of T600 and TNS*x*.

of the precursor NH_2-MIL-125 at 600 °C under the same heating rate and atmosphere without adding sulfur source) catalysts with large number of oxygen vacancies were obtained by high temperature calcination of NH_2-MIL-125 and sulfur powder in an air atmosphere. It is found that the cube-like S/N co-doped TiO_2 with rich oxygen vacancies exhibits efficient elimination performance for HCHO. The possible photocatalytic oxidation mechanism is explored by various characterization techniques.

The specific procedure for the preparation of TNS*x* samples after derivatization from NH_2-MIL-125 was described in Supporting information. The micro structure of NH_2-MIL-125, T600, and TNS600 were observed by SEM characterization. As shown in Fig. 1a, NH_2-MIL-125 presented a cubic shape with a particle size of about 600 nm, which was parallel to the record in the previous work [15]. Meanwhile, T600 and TNS600 were selected as the representative materials to explore the morphology changes after pyrolysis (Figs. 1b and c). It could be seen that after calcination, the original cubic shape derived from Ti-MOFs was well maintained for the T600 and TNS600 samples with the 400 nm of grain size.

The cubic particles were characterized by TEM to further understand the structural information. As seen in Fig. 1d, the particles had a cube-shaped structure that was similar to the shape shown in the SEM images. A high magnification investigation of individual cubic particle (Fig. 1e) showed that the surface was rough after calcination. Furthermore, HRTEM image showed very clear crystalline surface, and regular lattice stripes were observed. The interplanar spacings of 0.352 and 0.243 nm were marked in Fig. 1f, which was due to the anatase TiO_2 (101) and (103) phase, respectively. The obtained photocatalyst with cubic morphology exposed more reactive sites than the traditional agglomeration-prone microsphere morphology, which benefited the well contact of between the pollutants and the photocatalysts. We have also analyzed selected area electron diffraction (SAED) using spherical aberration electron microscopy as shown in Fig. 1g. SAED image showed the crystalline surface of anatase. Fig. 1h showed the EDS results of the TNS600 photocatalyst. It could be seen that Ti, O, S, C and N elements were uniformly dispersed on the surface of TNS600, further proving the successful preparation of doped photocatalysts TNS*x*. Finally, a combination of XRD (Figs. S1a and b in Supporting information) and FTIR (Figs. S1c and d in Supporting information) analyses together revealed the successful preparation of S/N-TiO_2. The doping of sulfur inhibited the formation of rutile phase. Anatase TiO_2 was superior to rutile TiO_2 in terms of photocatalytic ability [16,17]. In terms of photocatalytic ability, anatase TiO_2 was superior to rutile TiO_2 [18]. The anatase phase might be an important reason for the high photocatalytic activity of TNS*x*. The average crystallite size (D) was calculated as shown in Table S1 (Supporting information), demonstrating that sulfur doping reduced the particle size of the photocatalyst. And the actual content of S and Ti were quantified by X-ray fluorescence spectrometry (XRF). As shown in Table S1, the molar percentage of S/Ti firstly increased and then decreased as the calcination temperature increased, with the highest molar percentage of S/Ti at 600 °C and the maximum S doping of TNS600. The TNS*x* sample was also found to have a higher specific surface area by nitrogen adsorption-desorption analyses (Fig. S2 in Supporting information), which is shown in Table S1, which was more conducive to the separation of photogenerated electrons-vacancies. The presence of oxygen vacancies was confirmed by Raman analysis (Fig. S3a in Supporting information) and electron paramagnetic resonance (EPR) (Fig. S3b in Supporting information).

The valence state and surface composition of the T600 and TNS*x* samples were explored *via* the XPS technique. As shown in the Ti 2p spectra (Fig. 2a), the corresponding characteristic peak of Ti $2p_{1/2}$ and Ti $2p_{3/2}$ in TNS600 were located near 464.2 and 458.5 eV, suggesting the presence of Ti^{4+} [19]. The peaks at 457.2 and 463.0 eV were attributed to the Ti $2p_{3/2}$ and Ti $2p_{1/2}$ orbitals of Ti^{3+}, which confirmed the generation of Ti^{3+} on the surface, in consistent with the EPR results. Compared with T600, the binding energy of Ti in TNS*x* was shifted towards a higher binding energy, which was probably due to the different ionization energies of Ti and S. The electronegativity of S is higher than that of titanium, and the doping of S resulted in a lower electron density around Ti^{4+} [17,20]. In Fig. 2b, the characteristic peaks of S $2p_{3/2}$ at 168.6 eV and S $2p_{1/2}$ at 169.7 eV were well matched with the S^{6+} and S^{4+} species, which demonstrated that the sulfur doped into TNS*x* was distributed as S^{6+} and S^{4+} [17,21]. There was no S^{2-} characteristic peak located at 162.0 eV, further suggesting that the doping of sulfur was mainly cationic substitution of Ti species [21]. Ti^{4+} was replaced by S^{6+}/S^{4+} cation, generating impurity state in the gap between the valence and conduction band [21,22], which al-

lowed S doping to be photo-activated by light irradiation, thereby improving electron transfer efficiency [21,23].

The XPS O 1s spectra of TNS*x* were shown in Fig. 2c, where the three binding energies located at 528.7 eV, 531.3 eV and 533.1 eV of O component were divided into three species: lattice oxygen (O_{latt}), defect oxygen (O_{def}) and adsorbed oxygen (O_{ads}), respectively [24]. According to XPS O 1s analysis results in Table S2 (Supporting information), it can be concluded that during the heating process from 500 °C to 600 °C after doping S and N, the higher the temperature, the lower the content of O_{latt} species on the material surface and the higher the content of O_{def} species. This indicated that some lattice oxygen was lost and transformed into oxygen vacancy during the heating process, which was consistent with the EPR characterization. In addition, within the temperature range of 500–600 °C, increasing the temperature was beneficial for increasing the content of O_{ads} species on the surface of the material, resulting in the highest adsorbed oxygen content on the surface of TNS600 and the best catalytic performance. For TNS650 obtained by high-temperature calcination, compared with TNS600, its surface has a lower content of O_{def} species, indicating that the material surface contains fewer oxygen defects, and its O_{ads} species content was the lower, leading to a decrease in the surface's ability to capture formaldehyde molecules and a decrease in catalytic performance. The deconvolution of the N 1s peak revealed the presence of two peaks in Fig. 2d, assigned to N-doping and the formation of N-O-Ti species [25]. In addition, the atomic percentage of S and N were semi-quantitatively determined by XPS (Table S1). Similar to the XRF result, the S and N content firstly increased and then decreased as the calcination temperature increased, with the maximum doping of S and N at 600 °C.

The photocatalytic performance of the prepared S/N co-doped TiO_2 catalysts were investigated by xenon lamp irradiation. As shown in Fig. 3a, TNS600 showed excellent photooxidative capacity for HCHO removal within 150 min, with a removal rate of 98.00%, which was significantly higher than that (66.30%) of T600. Furthermore, the apparent reaction constant k values (Fig. 3b) for the photocatalytic degradation of HCHO over T600 and TNS*x* were calculated by the first-order kinetic model ($-\ln(C_t/C_0 = kt)$) [26]. It was arranged in the order of TNS600 ($0.02883 \pm 0.00043\ min^{-1}$) > TNS650 ($0.01200 \pm 0.00139\ min^{-1}$) > TNS500 ($0.00853 \pm 0.00063\ min^{-1}$) > T600 ($0.00744 \pm 0.00220\ min^{-1}$), indicating that the greater the S and N doping, the better the photocatalytic performance. The photocatalytic degradation activities of different photocatalysts for HCHO removal was summarized in Table S3 (Supporting information), and the present S/N-TiO_2 catalyst showed excellent photocatalytic activity. The reusability of TNS600 for HCHO removal was investigated under the same conditions, the removal efficiency over TNS600 decreased from 98.00% to 91.44% after 5 cycle experiment (Fig. S4 in Supporting information). The cycle experiment demonstrated the excellent stability of the TNS600 sample.

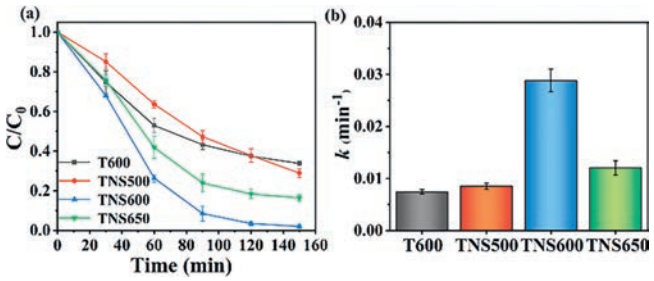

Fig. 3. Photocatalytic activities of various photocatalysts for HCHO removal by xenon lamp irradiation (a), and the corresponding apparent reaction constant k values (b).

Photoluminescence (PL) could characterize the carrier separation efficiency of photocatalysts (Fig. S5a in Supporting information) and time-resolved photoluminescence (TRPL) provided the charge carrier lifetime to assessed the separation efficiency of electron-hole pairs (Fig. S5b in Supporting information), both demonstrated the efficient separation of photogenerated electrons and holes in TNS600. The interfacial charge transfer efficiency of photocatalyst samples was compared based on the electrochemical impedance spectroscopy (EIS) test results (Fig. S5c in Supporting information). The photocurrent transient curves of T600 and TNS*x* were obtained through several turn on-off cycles (Fig. S5d in Supporting information). These results obtained from PL, TRPL, EIS and photocurrent transient curves above all came to the conclusion that TNS600 had the best photo generated carrier separation efficiency, which was in good agreement with TNS600 with the best photocatalytic performance.

EPR was selected for the detection of $^{\bullet}OH$ and $^{\bullet}O_2^-$ radicals. The active species of $^{\bullet}OH$ and $^{\bullet}O_2^-$ radicals of photocatalyst TNS600 were intercepted by DMPO using EPR as shown in Fig. S6 (Supporting information). No signal was detected in dark. Six characteristic peaks of DMPO-$^{\bullet}O_2^-$ due to the presence of $^{\bullet}O_2^-$ radicals and the characteristic 1:2:2:1 quadruple hydroxyl peaks due to the presence of $^{\bullet}OH$ radicals were examined after light irradiation for 5 min, respectively, indicating that $^{\bullet}O_2^-$ and $^{\bullet}OH$ radicals were produced on TNS600.

The band positions of TNS600 were calculated by the Mott-Schottky curve (Fig. S7 in Supporting information). The C^{-2} value of TNS600 was proportional to the potential, and thus TNS600 could be defined as an n-type semiconductor [27]. The flat band potential (E_{FB}) of TNS600 was −0.49 eV *vs.* Ag/AgCl obtained *via* the inverse extension of the curve from the two frequencies intersected on the x-axis. The property of the n-type semiconductor determined that its E_{FB} was 0.1 eV more positive than the conduction band potential (E_{CB}) [28]. After converting to the standard hydrogen electrode potential, the E_{CB} of TNS600 was calculated to be −0.39 eV *vs.* NHE. Combined with the band gaps of the two materials analyzed by UV-vis DRS (Fig. S8 in Supporting information), the valence band width (E_{VB}) of TNS600 was 2.91 eV *vs.* NHE, which was calculated *via* the formula ($E_g = E_{VB} - E_{CB}$). Since the E_{VB} of TNS600 was higher than the $OH^-/^{\bullet}OH$ with redox potential of 2.40 eV *vs.* NHE, the reaction of photogenerated holes h^+ combined with H_2O to produce $^{\bullet}OH$ could take place in the valence band of TNS600. Similarly, the E_{CB} of TNS600 was −0.39 eV *vs.* NHE, which was lower than the $O_2/^{\bullet}O_2^-$ with redox potential of –0.33 eV *vs.* NHE. Hence the reaction of photogenerated electrons e^- combined with O_2 to produce $^{\bullet}O_2^-$ could take place in the conduction band of TNS600 [29]. The photogenerated carriers participated in the generation process of oxidative radicals, inhibiting the recombination process to a certain extent, and enhancing the photocatalytic activity of TNS600.

To gain insight into the mechanism of HCHO oxidation on the catalyst, we carried out diffuse reflectance *in situ* IR testing and analysis of the TNS600 sample (Fig. S9 in Supporting information). We proposed a photocatalytic mechanism for HCHO removal by S/N-titanium dioxide, as shown in Fig. 4. The S/N-TiO_2 composite retained the unique structural of NH_2-MIL-125 and offered a large possibility for the transfer of photogenerated electrons and holes. After S/N-TiO_2 exposed to the xenon lamp, a large number of photogenerated carriers were generated over S/N-TiO_2 (Eq. 1). The electrons on the valence band first migrated to an intermediate band formed by oxygen vacancies (O_v) [30,31], and then were trapped leaving many holes on the valence band and achieving an effective separation of electrons and holes. The trapped electrons further transferred to the conduction band of the catalyst. The existence of oxygen vacancies in S/N-TiO_2 could significantly contribute to the generation of free radicals, and the electrons

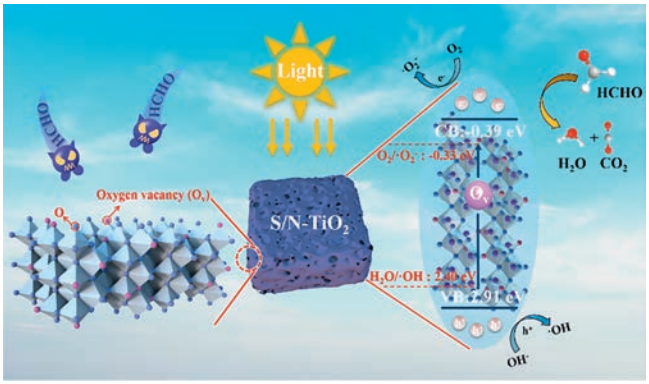

Fig. 4. Photocatalytic mechanism of S/N-TiO_2 for HCHO removal.

stored on the conduction band of S/N-TiO_2 could react with the adsorbed molecular oxygen to form $\cdot O_2^-$ radicals (Eq. 2). Photogenerated holes (h^+) retained on the valence band could further react with nearby water molecules or surface hydroxyl groups to form highly reactive $\cdot OH$ radicals (Eq. 3) [32]. Thus, formaldehyde oxidation may follow four steps: (1) Adsorption on the catalyst surface (Eq. 4); (2) adsorbed HCHO can be oxidized by tow radicals ($\cdot O_2^-$/$\cdot OH$) to produce DOM (H_2CO_2) (Eq. 5); (3) DOM is further oxidized to formate species and carbonate species (Eq. 6); and (4) complete mineralization of intermediate species to CO_2 and H_2O (Eq. 7) [33,34].

$$S/N\text{-}TiO_2 + h\nu \rightarrow S/N\text{-}TiO_2\ (h^+ + e^-) \quad (1)$$

$$O_2 + e^- \rightarrow \cdot O_2^- \quad (2)$$

$$-OH + h^+ \rightarrow \cdot OH \quad (3)$$

$$HCHO \rightarrow HCHO(ads) \quad (4)$$

$$HCHO(ads) + \cdot O_2^-/\cdot OH \rightarrow H_2CO_2 \quad (5)$$

$$H_2CO_2 + \cdot O_2^-/\cdot OH \rightarrow HCOO^-/CO_3^{2-} \quad (6)$$

$$HCOO^-/CO_3^{2-} + \cdot O_2^-/\cdot OH \rightarrow H_2O + CO_2 \quad (7)$$

In this study, S/N co-doped TiO_2 materials with a large number of oxygen vacancies were prepared by adding sulfur powder during calcination of titanium-based MOFs NH_2-MIL-125. The co-doped catalyst possessed anatase phase TiO_2 and exhibited cubic morphology derived from the NH_2-MIL-125 precursor. With a change in the calcination temperature, the separation efficiency of photogenerated carriers over the prepared photocatalysts also changed, due to the effect of calcination temperature on the S doping level in TNS*x*. Under xenon lamp irradiation, the photodegradation efficiency of HCHO within 150 min reached 98.00% over the TNS600 catalyst. Furthermore, the TNS600 catalyst possessed good recyclability. Not only the removal efficiency of HCHO, but also the morphology and crystal structure were well kept after 5 cycle experiment. The main reactive radicals involved in the photocatalytic oxidation reaction were the $\cdot O_2^-$ and $\cdot OH$ radicals. The S/N co-doped TiO_2 materials provided an idea for designing MOFs-derived photocatalysts for heterogeneous environmental remediation.

Declaration of competing interest

The authors declare that they have no known competing financial interests or personal relationships that could have appeared to influence the work reported in this paper.

Acknowledgment

This work was supported by the National Natural Science Foundation of China (Nos. 21876008 and 22276009).

Supplementary materials

Supplementary material associated with this article can be found, in the online version, at doi:10.1016/j.cclet.2023.109255.

References

[1] L. Xu, H. Zhang, P. Xiong, et al., Sci. Total. Environ. 753 (2021) 141975.
[2] Y. Feng, L. Dai, Z. Wang, et al., Environ. Sci. Technol. 56 (2022) 8722–8732.
[3] B. Robert, G. Nallathambi, Environ. Chem. Lett. 19 (2021) 2551–2579.
[4] Z. Soltanpour, Y. Mohammadian, Y. Fakhri, Environ. Res. 204 (2022) 112094.
[5] W. Ouyang, Y. Ji, S. Tan, et al., J. Alloys Compd. 866 (2021) 158964.
[6] B. Dong, T. Liu, C. Li, et al., Chin. Chem. Lett. 29 (2018) 671–680.
[7] Y. Li, Z. Yin, G. Ji, et al., Appl. Catal. B 246 (2019) 12–20.
[8] P.S. Basavarajappa, S.B. Patil, N. Ganganagappa, et al., Int. J. Hydrog. Energy 45 (2020) 7764–7778.
[9] X. Wang, L. Wu, Z. Wang, et al., Appl. Catal. B 322 (2023) 122075.
[10] Y. Wang, Q. Li, M. Deng, et al., Chin. Chem. Lett. 33 (2022) 324–327.
[11] Y.C. Zhou, P. Wang, H. Fu, et al., Chin. Chem. Lett. 31 (2020) 2645–2650.
[12] C.H. Hendon, D. Tiana, M. Fontecave, et al., J. Am. Chem. Soc. 135 (2013) 10942–10945.
[13] M.A. Nasalevich, R. Becker, E.V. Ramos-Fernandez, et al., Energy Environ. Sci. 8 (2015) 364–375.
[14] J. Chen, X. Zhang, F. Bi, et al., J. Colloid Interface Sci. 571 (2020) 275–284.
[15] S. Hu, M. Liu, K. Li, et al., CrystEngComm 16 (2014) 9645–9650.
[16] S. Liu, X. Chen, J. Hazard. Mater. 152 (2008) 48–55.
[17] M. Zhang, F. Meng, S. Zhang, et al., Chem. Eng. J. 429 (2022) 132475.
[18] D.A.H. Hanaor, C.C. Sorrell, J. Mater. Sci. 46 (2010) 855–874.
[19] G. Lu, X. Huang, Y. Li, et al., J. Energy Chem. 43 (2020) 8–15.
[20] W. Zhao, Q. Zhong, Y. Pan, et al., Chem. Eng. J. 228 (2013) 815–823.
[21] T. Li, A. Abdelhaleem, W. Chu, et al., Chem. Eng. J 411 (2021) 128450.
[22] S. Abu Bakar, C. Ribeiro, J. Mol. Catal. A: Chem. 412 (2016) 78–92.
[23] Y. Niu, M. Xing, B. Tian, et al., Appl. Catal. B 115-116 (2012) 253–260.
[24] X. Chen, B. Sun, J. Chu, et al., ACS Appl. Mater. Interfaces 14 (2022) 28945–28955.
[25] W. Ouyang, Y. Ji, Micro Nano Lett. 15 (2020) 566–569.
[26] X.H. Yi, H. Ji, C.C. Wang, et al., Appl. Catal. B 293 (2021) 120229.
[27] S. Hua, D. Qu, L. An, et al., Appl. Catal. B 240 (2019) 253–261.
[28] Y.X. Li, X. Wang, C.C. Wang, et al., J. Hazard. Mater. 399 (2020) 123085.
[29] X. Wei, C.C. Wang, Y. Li, et al., Chemosphere 280 (2021) 130734.
[30] J. Li, M. Zhang, Z. Guan, et al., Appl. Catal. B 206 (2017) 300–307.
[31] L. Hou, M. Zhang, Z. Guan, et al., Appl. Surf. Sci. 428 (2018) 640–647.
[32] Q. Huang, Y. Hu, Y. Pei, et al., Appl. Catal. B 259 (2019) 118106.
[33] M. Shabir, N. Shezad, I. Shafiq, et al., Ind. Eng. Chem. Res. 105 (2022) 539–548.
[34] H. Liu, Y. Ma, J. Chen, et al., Appl. Catal. B 250 (2019) 337–346.